Control of Knock-On Damage for 3D Atomic Scale Quantification of Nanostructures: Making Every Electron Count in Scanning Transmission Electron Microscopy

Sandra Van Aert,[1,*] Annick De Backer,[1] Lewys Jones,[2,3,4] Gerardo T. Martinez,[1,2] Armand Béché,[1] and Peter D. Nellist[2]
[1]*EMAT, University of Antwerp, Groenenborgerlaan 171, 2020 Antwerp, Belgium*
[2]*Department of Materials, University of Oxford, 16 Parks Road, Oxford OX1 3PH, United Kingdom*
[3]*Advanced Microscopy Laboratory, Centre for Research on Adaptive Nanostructures and Nanodevices (CRANN), Dublin 2, Ireland*
[4]*School of Physics, Trinity College Dublin, The University of Dublin, Dublin 2, Ireland*

(Received 13 July 2018; revised manuscript received 14 January 2019; published 13 February 2019)

Understanding nanostructures down to the atomic level is the key to optimizing the design of advanced materials with revolutionary novel properties. This requires characterization methods capable of quantifying the three-dimensional (3D) atomic structure with the highest possible precision. A successful approach to reach this goal is to count the number of atoms in each atomic column from 2D annular dark field scanning transmission electron microscopy images. To count atoms with single atom sensitivity, a minimum electron dose has been shown to be necessary, while on the other hand beam damage, induced by the high energy electrons, puts a limit on the tolerable dose. An important challenge is therefore to develop experimental strategies to optimize the electron dose by balancing atom-counting fidelity vs the risk of knock-on damage. To achieve this goal, a statistical framework combined with physics-based modeling of the dose-dependent processes is here proposed and experimentally verified. This model enables an investigator to theoretically predict, in advance of an experimental measurement, the optimal electron dose resulting in an unambiguous quantification of nanostructures in their native state with the highest attainable precision.

DOI: 10.1103/PhysRevLett.122.066101

In order to fully exploit structure-property relations of nanomaterials, three-dimensional (3D) characterization at the atomic scale is often required. The resolution of electron tomography has reached the atomic scale [1–3]. However, for most nanostructures, it is far from straightforward to acquire a large number of projection images since samples tend to degrade or deform under the electron beam. The time-consuming data acquisition and data processing steps are also not compatible with the high throughput needed to provide statistically meaningful results when there is natural variability, e.g., in catalyst samples. Therefore, estimation of 3D models from single 2D annular dark field (ADF) scanning transmission electron microscopy (STEM) images using atom counting has recently gained renewed interest [4–8]. In combination with prior knowledge about a material's crystal structure, an initial 3D configuration is then generated. Next, an energy minimization using *ab initio* calculations [6] or a Monte Carlo approach [7–9] is performed to relax a nanoparticle's 3D structure. The reliability of the reconstructed 3D model is set by the atom-counting precision, which in general will improve with increasing electron dose ensuring a better signal-to-noise ratio. However, with increasing electron dose, problems related to the stability and integrity of the material under study can be expected [10]. This is important when investigating beam-sensitive samples such as organic perovskites, colloidal semiconductors, ultrasmall clusters, or battery materials, but even for beam-hard materials, changes in the atomic structure may not be apparent visually and thus go unnoticed. Therefore, it is of great importance to determine the optimal electron dose for which atom-counting precision and radiation damage are balanced against each other. Moreover, finding the optimal instrumental settings is critical when performing environmental or *in situ* electron microscopy where any unintended influence of beam damage on the results should be avoided. In this Letter, a novel statistical methodology is proposed that can be used to predict the optimal dose and to detect the presence (or absence) of beam damage.

To count the number of atoms, so-called column-integrated scattering cross sections (SCSs) have been introduced in ADF STEM corresponding to the total fraction of scattered intensity attributed to each atomic column. These can be measured using statistical parameter estimation theory [1,11–13] or by integrating intensities over the probe positions in the vicinity of a single column of atoms [7,14]. As compared with other metrics, such as peak intensities, column-integrated SCSs are highly sensitive to thickness [15]. Moreover, they are robust to magnification, defocus, source size, astigmatism, and small sample mistilt [14,16,17]. Column-integrated SCSs have been measured from a dose series of high angle ADF (HAADF) STEM images of a Pt wedge sample viewed along the [110] zone axis. After 2 min of plasma cleaning, images were recorded

using a probe corrected FEI TITAN^3 equipped with a Wien filter monochromator operated at 300 keV, a 21 mrad semiconvergence angle, 58–190 mrad detector collection range, and pixel size of 9.1 pm. By defocusing the monochromator, the beam current was varied across 2 orders of magnitude over the range 1.4, 10, 25, 37, 50, and 150 pA, whereas the recording dwell time was kept fixed at 1 μs in order to ensure that unavoidable scan noise contributions remain constant. Moreover, the experimental intensities have been normalized with respect to the incident beam by taking the detector sensitivity into account [18,19]. In this manner, experimental column-integrated SCSs can be compared with libraries of simulated SCSs for which we have used the frozen lattice multislice approach [20]. As illustrative examples, images acquired at 1.4 and 37 pA are shown in Figs. 1(a) and 1(b) corresponding to an incident electron dose d of 1050 and 28 000 $e^-/\text{Å}^2$, respectively. These images can be modeled as a superposition of Gaussian functions using the StatSTEM software [13]. The refined models are shown in Figs. 1(c) and 1(d). From the estimated model parameters, column-integrated SCSs can be determined for each atomic column, which are represented in histograms in Figs. 1(e) and 1(f). They can be regarded as independent statistical draws from a Gaussian mixture model, i.e., a parametric probability density function represented as a weighted sum of Gaussian component densities [1,12]. The Gaussian mixture models, with their component locations matched to the simulated library values, are shown as an overlay in Figs. 1(e) and 1(f). Since the column-integrated SCSs scale with thickness, this Gaussian mixture model analysis can be used to assign atom counts to the atomic columns. The width of each Gaussian component, which is set by the finite electron dose and microscope instabilities, reflects the uncertainty in column-integrated SCSs and hence also in atom counts. The improvement in atom-counting reliability with increased electron dose is visualized in Figs. 1(g) and 1(h), where symmetrical 3D atom configurations based on the atom-counting results are shown. For metallic wedges, where smooth surface facets are expected, the presence of red-colored low-coordination atoms is indicative of likely atom-counting errors.

Although the atom-counting precision improves with increasing electron dose, the probability for knock-on displacement of atoms along the surface or even removal of atoms increases linearly with electron dose [10,21]. The importance of beam-induced atom displacement can in principle be tracked by comparing successive image frames. This works well for 2D materials, such as, graphene [22,23]. However, one needs to overcome the risk of directly associating beam damage to changes in atom counts since they may result as well from the inherently limited atom-counting precision shown in Fig. 1. Therefore, we developed a new analysis of variance method taking both the imprecision of column-integrated SCSs and structural damage into account. The method evaluates the amount of variation between column-integrated SCSs corresponding to successive frames i and j as a function of electron dose:

$$\begin{aligned} \text{var}_{\text{difference}} &= \text{var}(\text{SCS}^i_{n,g} - \text{SCS}^j_{n,h}) \\ &= 2\text{var}_{\text{within}} + \text{var}_{\text{between}}, \end{aligned} \tag{1}$$

where $\text{SCS}^i_{n,g}$ refers to the column-integrated SCS of the nth atomic column, having g atoms in frame i. The columns indexed by n are selected to be those containing g atoms in frame i. The same columns are used in frame j even though

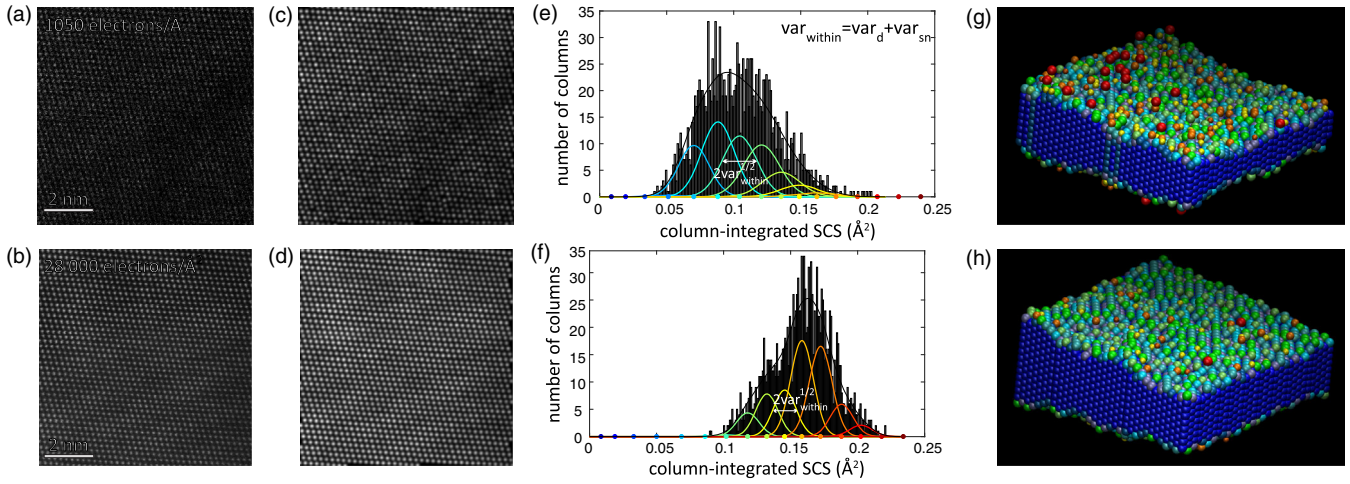

FIG. 1. (a),(b) Experimental HAADF STEM images of a Pt wedge sample along the [110] zone axis for an incident electron dose of 1050 and 28 000 $e^-/\text{Å}^2$. (c),(d) Refined parametric models of the images shown in (a),(b). (e),(f) Histograms of column-integrated SCSs for the images shown in (a),(b). The Gaussian mixture model is shown in black and the individual components, corresponding to different thicknesses, are shown in color. (g),(h) Symmetrical 3D atom configurations based on atom counting. The coloring of the atoms indicates the nearest neighbor coordination from 1 in red to 12 in blue.

the number of atoms in that column might have changed. Both the precision with which column-integrated SCSs can be measured within a single frame, $\mathrm{var}_{\mathrm{within}}$, and an extra variance related to effective changes in the number of atoms between two frames, $\mathrm{var}_{\mathrm{between}}$, contribute to $\mathrm{var}_{\mathrm{difference}}$ (see Supplemental Material [24] for more details). If the dominant beam damage mechanism is knock-on surface displacement, the variance between frames equals

$$\mathrm{var}_{\mathrm{between}} = 2P(\mathrm{sd})\delta^2, \tag{2}$$

where δ is the difference in mean column-integrated SCSs if the number of atoms in a column is changed by one atom (see Supplemental Material [24] for more details). The probability for surface displacement $P(\mathrm{sd})$ can be expressed as follows:

$$\begin{aligned} P(\mathrm{sd}) &= P(\mathrm{sd}|\mathrm{ad})P(\mathrm{ad}) + P(\mathrm{sd}|\overline{\mathrm{ad}})P(\overline{\mathrm{ad}}) \\ &\approx P(\mathrm{sd}|\mathrm{ad})P(\mathrm{ad}) \approx \sigma_{\mathrm{sd}} d \frac{N_{\mathrm{ad}}}{N_{\mathrm{col}}} \end{aligned} \tag{3}$$

where $P(\mathrm{sd}|\mathrm{ad})$ is the probability for surface displacement given an "adatom" lying on top of a surface and $P(\mathrm{sd}|\overline{\mathrm{ad}})$ is the probability for surface displacement given an atom lying within a surface plane. The probability $P(\mathrm{sd}|\overline{\mathrm{ad}})$ is assumed to be small as compared to $P(\mathrm{sd}|\mathrm{ad})$ since extra energy is required if an atom needs to be promoted first to an adatom site before it can be displaced along the surface [21]. The probability $P(\mathrm{ad})$ for an adatom equals the number of adatoms N_{ad} divided by the total number of atomic columns N_{col}. Following Ref. [21], the probability $P(\mathrm{sd}|\mathrm{ad})$ scales with the incoming electron dose d and the knock-on cross section σ_{sd} for which an analytical expression exists when using the Rutherford formula:

$$\sigma_{\mathrm{sd}} = (0.25\mathrm{b})FZ^2\left(\frac{1}{\sin^2(\theta_{\mathrm{min}}/2)} - \frac{1}{\sin^2(\theta_{\mathrm{max}}/2)}\right) \tag{4}$$

with $F = [1-(v/c)^2]/(v/c)^4$ (where v is the incident electron speed and c the speed of light) and Z the atomic number. The minimum and maximum angle resulting in scattering along the surface are given by

$$\begin{aligned} \theta_{\mathrm{min}} &= \arcsin\left[2(E_{\mathrm{sd}}/E_{\mathrm{max}})^{1/2}\right] \\ \theta_{\mathrm{max}} &= \pi - \arcsin\left[2(E_{\mathrm{sd}}/E_{\mathrm{max}})^{1/2}\right] \end{aligned} \tag{5}$$

with E_{sd} the surface diffusion energy and $E_{\mathrm{max}}(\mathrm{eV}) \approx (1.1/A)[2 + E_0/(511\ \mathrm{keV})]E_0(\mathrm{keV})$ (where A is the mass number and E_0 the incident electron energy).

The contribution $\mathrm{var}_{\mathrm{within}}$ in Eq. (1) describes the precision with which column-integrated SCSs can be measured from a single frame and corresponds to the variance of the Gaussian component densities as illustrated in Figs. 1(e) and 1(f). The precision is limited by the finite electron dose used to acquire an image as well as microscope instabilities, such that

$$\mathrm{var}_{\mathrm{within}} = \mathrm{var}_{\mathrm{d}} + \mathrm{var}_{\mathrm{sn}} \tag{6}$$

with $\mathrm{var}_{\mathrm{d}}$ the dose-dependent variance and $\mathrm{var}_{\mathrm{sn}}$ the dose-independent variance, which is mainly set by scan noise [25]. At first sight, both contributions appear to not be able to be uncoupled from a single image. However, by subsampling images, i.e., by taking every second pixel in both scan directions, an image is formed under identical scan noise conditions but where only one quarter of the total electron dose is used [26]. This leads to the opportunity to measure the dose-dependent variance and to compare this result with the expected outcome if only Poisson noise would contribute. Figures 2(a) and 2(b) show scatter plots of the column-integrated SCSs obtained before and after subsampling for an incident electron dose of 1050 and 28 000 $e^-/\mathrm{Å}^2$, respectively. In the absence of dose-dependent contributions, the column-integrated SCSs before and after subsampling would be identical and all points would lie on the bisector which is shown as a black line. Variations in differences of column-integrated SCSs before and after subsampling can therefore be attributed to dose related effects only and are reflected by the spread of data points around the bisector. When comparing Figs. 2(a) and 2(b), it is clear that this variation increases with decreasing electron dose as well as increasing column-integrated SCSs. More specifically, in the presence of Poisson noise only, it can be shown that

$$\mathrm{var}_{\mathrm{d}} \approx \frac{1}{3}\mathrm{var}(\mathrm{SCS}^{i}_{n,g} - \mathrm{SCS}'^{i}_{n,g}) \approx \frac{\mu_g}{d} \tag{7}$$

with $\mathrm{SCS}^{i}_{n,g}$ and $\mathrm{SCS}'^{i}_{n,g}$ the column-integrated SCSs before and after subsampling, respectively, and μ_g the mean column-integrated SCS for an atomic column with g atoms (see Supplemental Material [24]). Figures 2(a) and 2(b)

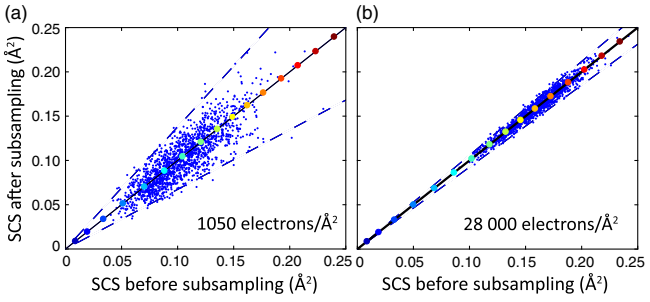

FIG. 2. Column-integrated SCSs before and after subsampling for an incident electron dose of (a) 1050 and (b) 28 000 $e^-/\mathrm{Å}^2$. The dashed black lines are at a distance of $\pm 3\sqrt{3\mu_g/d}$ from the bisector. The colored dots correspond to the simulated SCSs for increasing number of atoms in a column.

show that the differences between column-integrated SCSs before and after subsampling fall within approximately 3 times $\sqrt{3\mu_g/d}$ as expected for a normal distribution where 99% of the measurements lie within 3 times the standard deviation. This demonstrates the validity of a downsampled analysis to measure the dose-dependent variance and proves that the dose-dependent variations in image intensities are Poisson distributed, which is typical for electron counting detectors.

When combining Eqs. (1)–(7), it follows that the variance between column-integrated SCSs corresponding to successive image frames equals

$$\mathrm{var}_{\mathrm{difference}} = 2\frac{\mu_g}{d} + 2\mathrm{var}_{\mathrm{sn}} + 2\sigma_{\mathrm{sd}}\frac{N_{\mathrm{ad}}}{N_{\mathrm{col}}}\delta^2 d. \qquad (8)$$

This expression shows the contributions of Poisson noise, scan noise, and structural damage, being inversely proportional, constant, and linear with d, respectively. By varying the beam current between 1.4 and 150 pA, variances could be determined experimentally as a function of electron dose by measuring column-integrated SCSs from successive images. Following Eq. (8), the experimental variance depends on the number of atoms g in an atomic column. Since all images of the beam current series correspond to slightly different areas of the sample, a common thickness needs to be determined for which 10 atoms has been found to be present most frequently. The experimentally measured variances, shown by black error bars in Fig. 3, are therefore based on columns for which the number of atoms equals 10 in the first frame. Since beam currents larger than 150 pA could not be achieved experimentally without losing spatial resolution, the results corresponding to the 9 largest dose values have been obtained by comparing image numbers 2 to 10 with respect to image number 1 of a time series of 10 images. The black curve shows the evaluation of the right-hand side of Eq. (8) as a function of electron dose with the parameters μ_g, $\mathrm{var}_{\mathrm{sn}}$, and σ_{sd} estimated from the experimental variances using a weighted least squares optimization. The number of adatoms in Eq. (8) has been taken equal to the number of atoms with coordination number less than or equal to 6, and therefore do not include atoms within a clean surface. The estimated value for the mean column-integrated SCS, $\hat{\mu}_g = 0.1451 \pm 0.0091$ Å^2, is in excellent agreement with the expected value resulting from multislice image simulations for a 10 atoms thick column, $\mu_g = 0.1456$ Å^2. Although Fig. 3 shows that Poisson noise is limiting the atom-counting reliability for low values of the electron dose, scan noise plays a dominant role when the dose surpasses a value of only 2×10^3 $e^-/$Å^2. The experimentally measured dose-independent contribution scales linearly with μ_g and equals $\hat{\mathrm{var}}_{\mathrm{sn}} = (6.59 \pm 0.75) \times 10^{-5}$ Å^4 for a 10 atoms thick column. In the case of a 10-frame series, this can be reduced by approximately 45% when correcting for scan noise using nonrigid registration [25]. From Fig. 3, it is clear that even for a stable Pt wedge sample, beam damage starts to play a significant role for electron doses from around 2×10^5 $e^-/$Å^2, which is commonly used in practice. The method also enables us to measure the cross section for surface displacement, $\hat{\sigma}_{\mathrm{sd}} = (7.35 \pm 2.01) \times 10^{-7}$ Å^2, from which an experimental value for the surface diffusion energy follows, $\hat{E}_{\mathrm{sd}} = 1.09 \pm 0.01$ eV, when using Eqs. (4) and (5). This value is in good agreement with the theoretically predicted value for surface displacement of Pt atoms on a (110) Pt substrate, $E_{\mathrm{sd}} = 1.07$ eV [27].

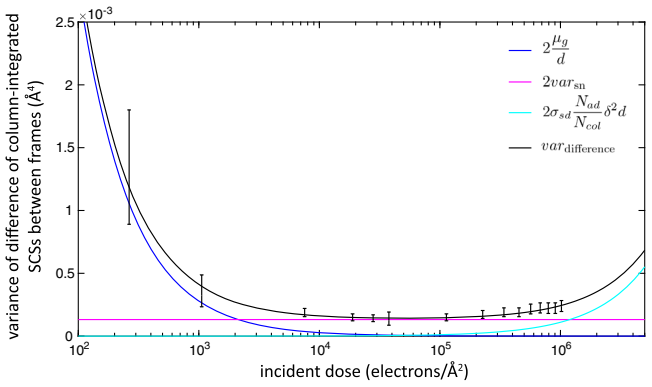

FIG. 3. Experimentally measured variances between column-integrated SCSs of two successive image frames are shown in black. The number of atoms equals 10 in the first frame. Error bars represent one standard deviation. The black curve shows the evaluation of the right-hand side of Eq. (8) with the contributions of Poisson noise, scan noise, and structural damage in blue, purple, and cyan, respectively.

The theoretical model, which we have validated experimentally, cannot only be used to measure physical parameters, such as, the surface diffusion energy. Minimization of Eq. (8) as a function of d also enables one to predict the optimal electron dose which balances atom-counting reliability vs the risk of structural damage:

$$d_{\mathrm{optimal}} = \sqrt{\frac{\mu_g}{\sigma_{\mathrm{sd}}\frac{N_{\mathrm{ad}}}{N_{\mathrm{col}}}\delta^2}}. \qquad (9)$$

Using this analytical expression, the optimal dose has been computed for different combinations of adatoms on a substrate and microscope settings as shown in Table I. These predicted values can be compared against the experimental imaging conditions used in state-of-the-art STEM experiments where the atomic structure of Pt [28] and Au [29] nanoparticles has been characterized and where single N atoms on graphene have been detected [30]. This comparison suggests the possibility to reduce the electron dose by a factor of approximately 100, thus significantly decreasing the probability for beam-induced surface diffusion, $\sigma_{\mathrm{sd}} d_{\mathrm{optimal}}$. Moreover, a further reduction

TABLE I. Predicted values for the optimal electron dose (d_{optimal}), atom-counting reliability both in the presence and absence of scan noise ($\sqrt{\mathrm{var}_d + \mathrm{var}_{\mathrm{sn}}}/\delta$), and probability for beam-induced surface diffusion ($\sigma_{\mathrm{sd}} d_{\mathrm{optimal}}$) for different adatoms on a substrate and microscope settings.

	Pt on 10 atoms thick (110) Pt substrate	Pt on 10 atoms thick (100) Pt substrate	Pt on 10 atoms thick (100) Pt substrate	Au on 10 atoms thick (100) Au substrate	N on graphene	N on graphene	H on graphene
E_{sd} (eV)	1.07 [27]	0.61 [32]	0.61 [32]	0.55 [33]	1.00 [34]	1.00 [34]	0.78 [35]
E_0 (keV)	300	300	200	200	60	60	60
Probe semiconvergence angle (mrad)	21	21	22	24	30	30	30
Detector collection range (mrad)	58–190 (HAADF)	58–190 (HAADF)	51–248 (HAADF)	54–270 (HAADF)	86–190 (HAADF)	40–190 (LAADF)	40–190 (LAADF)
d_{optimal} ($e^-/\mathrm{Å}^2$)	14 300	5090	4320	3380	9090	2710	18 620
Atom-counting reliability (for $\mathrm{var}_{\mathrm{sn}} = 4.5 \times 10^{-4} \mu_g$)	0.7	0.7	0.5	0.5	0.9	0.3	1.2
Atom-counting reliability (for $\mathrm{var}_{\mathrm{sn}} = 0$ Å^4)	0.2	0.4	0.3	0.3	0.4	0.2	0.4
$\sigma_{\mathrm{sd}} d_{\mathrm{optimal}}$ (%)	14	40	24	27	16	5	17

in electron dose combined with an increase in atom-counting reliability can be expected by optimizing the detector collection range, for which the low angle ADF (LAADF) regime has been found to be optimal for thin samples [31]. This is illustrated in Table I, where the atom-counting reliability is expressed as the relative width of neighboring Gaussian components of the Gaussian mixture model, i.e., the square root of Eq. (6) divided by the distance δ between those components (numbers larger than 1 imply unreliable atom counts). Moreover, the atom-counting reliability significantly improves in the absence of microscope instabilities. Following this new guidance to determine the optimal conditions opens up new opportunities for future experiments and predicts that even the detection of, e.g., H atoms on graphene becomes feasible. Finally, it is important to note that the predicted electron dose only reduces beam-induced displacements, which in general exceeds thermal motion for $E_{\mathrm{sd}} > 0.5$ eV. If E_{sd} is smaller than a temperature-dependent threshold value, thermal motion is likely to predominate [21].

In conclusion, a statistics-based analysis of variance method has been introduced to evaluate how the atom-counting precision as well as the probability for structural damage evolve as a function of electron dose. By modeling the underlying dose-dependent processes, a theoretical model has been proposed and experimentally verified to predict variations in column-integrated SCSs corresponding to successive image frames. In this manner, the presence or absence of knock-on damage can be detected. Moreover, this model can be used to predict the optimal electron dose to quantify unknown nanostructures in their native state with the highest precision before conducting the experiment. This is of critical importance when studying beam-sensitive nanostructures or when performing environmental or *in situ* electron microscopy where one should overcome any undesirable effect of knock-on damage.

This project has received funding from the European Research Council (ERC) under the European Union's Horizon 2020 research and innovation programme (Grant Agreement No. 770887). The authors acknowledge financial support from the Research Foundation Flanders (FWO, Belgium) through project fundings (WO.010.16N, G.0934.17N, G.0502.18N, G.0267.18N), and a grant to A. D. B. The research leading to these results has received funding from the European Union Seventh Framework Programme under Grant Agreement No. 312483—ESTEEM2 (Integrated Infrastructure Initiative-I3) and the UK EPSRC (Grant No. EP/M010708/1).

*Sandra.VanAert@uantwerpen.be

[1] S. Van Aert, K. J. Batenburg, M. D. Rossell, R. Erni, and G. Van Tendeloo, Nature (London) **470**, 374 (2011).
[2] B. Goris, S. Bals, W. Van den Broek, E. Carbo-Argibay, S. Gomez-Grana, L. M. Liz-Marzan, and G. Van Tendeloo, Nat. Mater. **11**, 930 (2012).
[3] R. Xu, C.-C. Chen, L. Wu, M. C. Scott, W. Theis, C. Ophus, M. Bartels, Y. Yang, H. Ramezani-Dakhel, M. R. Sawaya, H. Heinz, L. D. Marks, P. Ercius, and J. Miao, Nat. Mater. **14**, 1099 (2015).
[4] Z. Y. Li, N. P. Young, M. Di Vece, S. Palomba, R. E. Palmer, A. L. Bleloch, B. C. Curley, R. L. Johnston, J. Jiang, and J. Yuan, Nature (London) **451**, 46 (2008).
[5] J. M. LeBeau, S. D. Findlay, L. J. Allen, and S. Stemmer, Nano Lett. **10**, 4405 (2010).
[6] S. Bals, S. Van Aert, C. P. Romero, K. Lauwaet, M. J. Van Bael, B. Schoeters, B. Partoens, E. Yücelen, P. Lievens, and G. Van Tendeloo, Nat. Commun. **3**, 897 (2012).
[7] L. Jones, K. E. MacArthur, V. T. Fauske, A. T. J. van Helvoort, and P. D. Nellist, Nano Lett. **14**, 6336 (2014).
[8] A. De Backer, L. Jones, I. Lobato, T. Altantzis, B. Goris, P. D. Nellist, S. Bals, and S. Van Aert, Nanoscale **9**, 8791 (2017).

[9] T. Ellaby, J. Aarons, A. Varambhia, L. Jones, P. Nellist, D. Ozkaya, M. Sarwar, D. Thompsett, and C.-K. Skylaris, J. Phys. **30**, 155301 (2018).
[10] R. F. Egerton, P. Li, and M. Malac, Micron **35**, 399 (2004).
[11] S. Van Aert, J. Verbeeck, R. Erni, S. Bals, M. Luysberg, D. Van Dyck, and G. Van Tendeloo, Ultramicroscopy **109**, 1236 (2009).
[12] S. Van Aert, A. De Backer, G. T. Martinez, B. Goris, S. Bals, G. Van Tendeloo, and A. Rosenauer, Phys. Rev. B **87**, 064107 (2013).
[13] A. De Backer, K. H. W. van den Bos, W. Van den Broek, J. Sijbers, and S. Van Aert, Ultramicroscopy **171**, 104 (2016).
[14] H. E, K. E. MacArthur, T. J. Pennycook, E. Okunishi, A. J. D'Alfonso, N. R. Lugg, L. J. Allen, and P. D. Nellist, Ultramicroscopy **133**, 109 (2013).
[15] G. T. Martinez, K. H. W. van den Bos, M. Alania, P. D. Nellist, and S. Van Aert, Ultramicroscopy **187**, 84 (2018).
[16] G. T. Martinez, A. Rosenauer, A. De Backer, J. Verbeeck, and S. Van Aert, Ultramicroscopy **137**, 12 (2014).
[17] K. E. MacArthur, A. J. D'Alfonso, D. Ozkaya, L. J. Allen, and P. D. Nellist, Ultramicroscopy **156**, 1 (2015).
[18] A. Rosenauer, K. Gries, K. Müller, A. Pretorius, M. Schowalter, A. Avramescu, K. Engl, and S. Lutgen, Ultramicroscopy **109**, 1171 (2009).
[19] T. Grieb, K. Müller, R. Fritz, M. Schowalter, and A. Rosenauer, Ultramicroscopy **117**, 15 (2012).
[20] A. Rosenauer and M. Schowalter, in *Microscopy of Semiconducting Materials 2007* (Springer, New York, 2008), pp. 170–172.
[21] R. F. Egerton, Microsc. Microanal. **19**, 479 (2013).
[22] J. C. Meyer, F. Eder, S. Kurasch, V. Skakalova, J. Kotakoski, H. J. Park, S. Roth, A. Chuvilin, S. Eyhusen, G. Benner, A. V. Krasheninnikov, and U. Kaiser, Phys. Rev. Lett. **108**, 196102 (2012).
[23] T. Susi, J. Kotakoski, D. Kepaptsoglou, C. Mangler, T. C. Lovejoy, O. L. Krivanek, R. Zan, U. Bangert, P. Ayala, J. C. Meyer, and Q. Ramasse, Phys. Rev. Lett. **113**, 115501 (2014).
[24] See Supplemental Material at http://link.aps.org/supplemental/10.1103/PhysRevLett.122.066101 for a detailed derivation of the expressions of the statistical variances.
[25] L. Jones, H. Yang, T. J. Pennycook, M. S. J. Marshall, S. Van Aert, N. D. Browning, M. R. Castell, and P. D. Nellist, Adv. Struct. Chem. Imaging **1**, 8 (2015).
[26] A. De Backer, G. T. Martinez, K. E. MacArthur, L. Jones, A. Béché, P. D. Nellist, and S. Van Aert, Ultramicroscopy **151**, 56 (2015).
[27] T. Halicioglu and G. M. Pound, Thin Solid Films **57**, 241 (1979).
[28] J. Aarons, L. Jones, A. Varambhia, K. E. MacArthur, D. Ozkaya, M. Sarwar, C. K. Skylaris, and P. D. Nellist, Nano Lett. **17**, 4003 (2017).
[29] A. B. Yankovich, B. Berkels, W. Dahmen, P. Binev, and P. M. Voyles, Adv. Struct. Chem. Imaging **1**, 2 (2015).
[30] J. H. Warner, Z. Liu, K. He, A. W. Robertson, and K. Suenaga, Nano Lett. **13**, 4820 (2013).
[31] A. De Backer, A. De wael, J. Gonnissen, and S. Van Aert, Ultramicroscopy **151**, 46 (2015).
[32] R. M. Lynden-Bell, Surf. Sci. **259**, 129 (1991).
[33] K. Pötting, W. Schmickler, and T. Jacob, ChemPhysChem **11**, 1395 (2010).
[34] K. Nakada and A. Ishii, Solid State Commun. **151**, 13 (2011).
[35] C. P. Herrero and R. Ramírez, J. Phys. D **43**, 255402 (2010).